NANO LETTERS



pubs.acs.org/NanoLett
Letter

# Nanoscale Imaging of Palladium-Enhanced Photocatalytic Reduction of 4-Nitrothiophenol on Tungsten Disulfide Nanoplates

Swati J. Patil and Dmitry Kurouski*

Cite This: *Nano Lett.* 2024, 24, 13004−13009
Read Online



**ABSTRACT:** Two-dimensional (2D) dichalcogenides are modern nanomaterials with unique physical and chemical properties. These materials possess band gaps in the infrared and visible regions of the electromagnetic spectrum that can be tuned by their molecular composition. Excitons generated as a result of such light-matter interactions are capable of catalyzing chemical reactions in molecular analytes present on the dichalcogenide surfaces. However, the photocatalytic properties of such nanomaterials remain poorly understood. In the current study, we utilize tip-enhanced Raman spectroscopy (TERS) to examine photocatalytic reduction of 4-nitrothiophenol (4-NTP) to *p,p′*-dimercaptoazobisbenzene (DMAB) on tungsten disulfide ($WS_2$) nanoplates and $WS_2$ coupled with palladium nanoparticles ($WS_2$@PdNPs). Our results indicate that although both $WS_2$ and $WS_2$@Pd were capable of reducing 4-NTP into DMAB, the metallic hybrid demonstrated much greater yield and rates of DMAB formation compared to $WS_2$ nanoplate. These results indicate that coupling of catalytic metals to dichalcogenides could be used to enhance their catalytic properties.

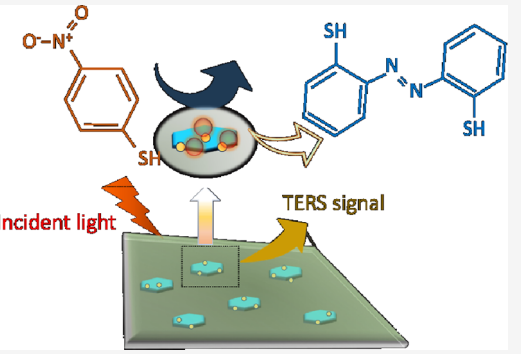


**KEYWORDS:** *Tungsten disulfide, palladium, photocatalysis, TERS imaging*



Metallic nanostructures formed by plasmonic and non-plasmonic metals demonstrate strong absorption properties in the visible and infrared parts of electromagnetic spectrum.[1−3] Light absorption generates coherent oscillations of conductive electrons on their surfaces, also known as localized surface plasmon resonances (LSPRs).[4,5] LSPRs determine $10^6$−$10^8$ enhancement of Raman scattering from molecules present in the close proximity to such nanostructure, a phenomenon known as surface-enhanced Raman scattering.[6,7] LSPRs can decay producing heat or decay via nonradiative pathways producing hot carriers.[8,9] These highly energetic short-living species can be directly or indirectly injected into molecular orbitals of molecules present on the metal surfaces and, consequently, trigger chemical transformations.[10,11] During the past decade, a substantial amount of evidence was accumulated about such plasmon-driven transformations.[12,13] Furthermore, it was found that coupling of plasmonic nanostructures with catalytic metals, such as platinum (Pt) or palladium (Pd), allows for the substantial expansion of the chemical reactions that could be catalyzed by such bimetallic nanoreactors.[14−18]

During the past decade, substantial advances have been made in the fabrication of two-dimensional (2D) dichalcogenides.[35] These modern nanomaterials possess unique physical and chemical properties due to simplicity of their fabrication, unique light-metal coupling and tunable band gaps in visible and infrared parts of electromagnetic spectrum.[12,19] 2D dichalcogenides became broadly used in optoelectronics applications[26] such as light sources,[27] optical modulators,[28] photodetectors,[29] field-effect transistors,[30] logic circuits,[31] sensors[32−34] etc.[20−22] Furthermore, 2D dichalcogenides exhibit unique catalysts and optoelectronics properties. For instance, An et al.[25] found that a MXene-based Au@Ag@Pd/$Ti_3C_2$ photocatalyst could be used for light-driven hydrogenation of nitroaromatics. Lambin and co-workers found that molybdenum disulfide ($MoS_2$) flakes could catalyze photocatalytic reduction of 4-nitrobenzenethiol (4-NBT) to *p,p′*-dimercaptoazobisbenzene (DMAB),[19] a chemical reaction that was previously evident only for plasmonic metals.[20] Expanding upon this, we utilized tip-enhanced Raman spectroscopy (TERS) to examine catalytic properties of tungsten disulfide ($WS_2$) nanoplates, as well as $WS_2$ coupled with palladium nanoparticles ($WS_2$@Pd). In TERS, scanning probes could be brought in the close proximity to the surface of 2D materials.[1−4] Next, the apex of the scanning probe is illuminated by a laser light. This generates LSPRs at the metal surface.[5−12] LSPRs enhance Raman scattering from the molecules located directly under the tip. This provides TERS

**Received:** July 31, 2024
**Revised:** September 25, 2024
**Accepted:** September 27, 2024
**Published:** October 7, 2024

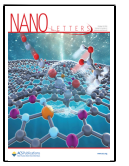





https://doi.org/10.1021/acs.nanolett.4c03702
*Nano Lett.* 2024, 24, 13004−13009

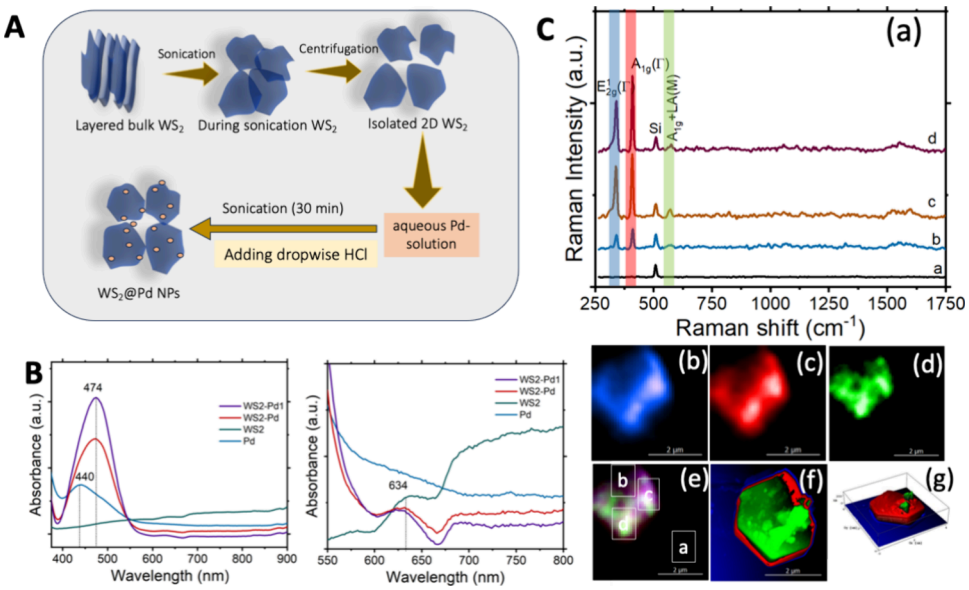


**Figure 1.** Synthesis and physical properties of $WS_2$. A. The scheme of synthetic approaches used for the fabrication of $WS_2$@PdNPs; B. UV−visible spectra of $WS_2$ and $WS_2$@PdNPs; C. (a) TER spectra of the $WS_2$ nanoplate. (b-e) TERS image of $WS_2$ nanoplate with $E^1_{2g}$ (blue), $A_{1g}$ (red) and $A_{1g}$+LA(M) (green) bands. (f) TERS image of $WS_2$ from overlapping $E_{2g}$, $A_{1g}$ and $A_{1g}$+LA(M) vibrations. (g) Corresponding AFM image of $WS_2$ nanoplate.

single-molecule sensitivity.[13,14] Furthermore, the electric field is confined under the tip down to a pico-volume enabling subnanometer spatial resolution in TERS imaging.[13,21−23] t

A chemical approach was used for the $WS_2$@NPs synthesis. The commercially available stacked tungsten disulfide ($WS_2$) nanoplatelets (Sigma-Aldrich) were further modified in ethanolic solution to separate the nanoplates, Figure 1, A. The $WS_2$ stacked layers were added to the ethanolic solution and subjected to sonication for 4 h so that 2D $WS_2$ suspensions formed. Further, it was centrifuged at 10000 rpm for 15 min in ethanol. The formed 2D dichalcogenides are typically seen as an interlayer of S and W atoms stabilized by van der Waals forces. Next, $WS_2$ nanoplates were mixed with PdNPs to synthesize $WS_2$@Pd hybrids, Figure 1, A. PdNPs were prepared with ascorbic acid (10 mM) and subsequentially added $H_2PdCl_4$ (5 mM), followed by stirring for 30 s. Further, $WS_2$ nanoplates (250 $\mu$L) were mixed with the above solution by stirring for 10 s, and the above mixture was kept at room temperature for 30 min until the Pd layer formed on the top of the $WS_2$ nanoplates. In the final step, the solution was centrifuged under water and ethanol for 5 min at 5000 rpm, redispersed in ethanol, and sonicated for over 20 s to form the final $WS_2$@Pd hybrids. UV−vis spectroscopy revealed that $WS_2$ had an absorption band at ∼634 nm, Figure 1, B, whereas $WS_2$@Pd exhibited the absorption ∼474 nm, originating from the absorbance of PdNPs evident at 440 nm. The 34 nm red shift points to the coupling between $WS_2$ and PdNPs.

We also used TERS to examine the crystalline properties of $WS_2$. We observed three vibrational bands in the acquired TERS spectra that corresponded to $E^1_{2g}$ (M) mode at 355 $cm^{-1}$; $A_{1g}$ ($\tau$) mode at 417 $cm^{-1}$ and $A_{1g}$ × LA(M) at 582 $cm^{-1}$, Figure 1, C. The strong in-plane $E^1_{2g}$ mode originated from the out-of-plane vibrations of S atoms relative to the W atoms. $A_{1g}$ ($\tau$) mode could be assigned to the out-of-plane vibration of S atoms, Figure 1, C, panel (a). The vibrational mode ∼417 $cm^{-1}$ originated from the second-order process that involved the longitudinal acoustic phonons at the M point (LA(M)). Strong intensity of the LA(M) vibration in the acquired TER spectra indicated the multilayered nature of the synthesized $WS_2$ nanosheets. TER maps of $E^1_{2g}$ (blue-pixel), $A_{1g}$ ($\tau$) (green-pixel), and 2 × LA(M) (red-pixel) was displayed in Figure 1, C, panels (b), (c), and (d), respectively and corresponding atomic force microscopy (AFM) image as shown in Figure 1, C, panel (f). We also found that $WS_2$@PdNPs exhibited crystalline properties similar to those of $WS_2$, Figure S1.

Next, we exposed $WS_2$ nanoplates adsorbed onto silicon (Si) wafer to an ethanolic solution of 4-NTP. After several seconds of exposure, the excess of 4-NTP was removed by extensive rinsing of $WS_2$ nanoplates with pure ethanol. Next, $WS_2$ nanoplates were dried under a nitrogen flow and analyzed using TERS. 4-NTP has a distinct vibrational band at 1069, 1098, 1330, and 1563 $cm^{-1}$ that were observed in TERS spectra collected at different sites of $WS_2$ nanoplates, Figure 2. We also found that TERS spectra acquired in the central part of the $WS_2$ nanoplates exhibited a doublet at 1437 and 1468 $cm^{-1}$ that could be assigned to DMAB.[24,25] These results indicate that $WS_2$ nanoplates were able to reduce 4-NTP into DMAB. Although the exact mechanism of DMAB formation on $WS_2$ is unclear, our previous study suggests that high reactivity of $NO_2$ group was determined by its low photopotential.[26] Density functional theory calculations also showed that 4-NTP would uptake two electrons and two protons from the monolayer of water present on the surface of such nanostructures at ambient conditions.[26] As a result, the $NO_2$ group would be reduced to NO and then to NHOH. However, the following reduction of NHOH to $NH_2$ is thermodynamically unfavorable compared to dimerization of two molecules that possess NHOH groups into the molecule with one azo bond (DMAB).

Our results also indicate that reactivity of the central parts of $WS_2$ nanoplates was greater than the reactivity at the edges of these nanomaterials. One can expect that a scanning probe exposed to the nanostructure surfaces could be responsible for


https://doi.org/10.1021/acs.nanolett.4c03702
Nano Lett. 2024, 24, 13004−13009

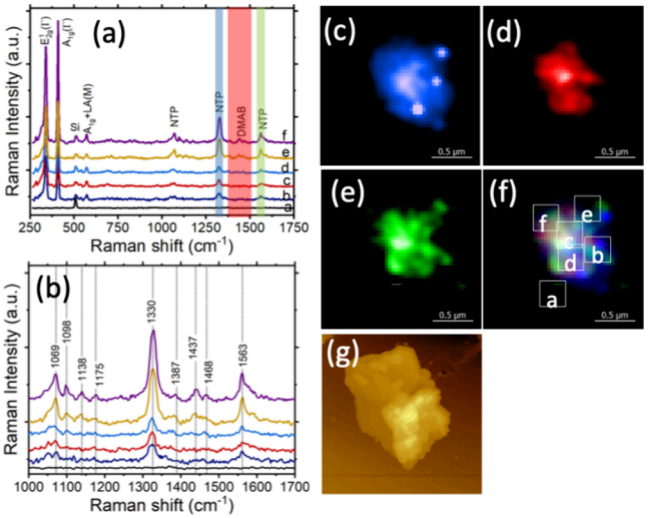


**Figure 2.** Catalytic reactivity of $WS_2$ nanoplates. (a) TER spectra extracted from chemical maps on 4-NTP decorated $WS_2$ nanoplate: (b) showing presence of 4-NTP and DMAB. (c–f) TERS image of $WS_2$ with (c) and (e) 4-NTP and (d) DMAB. (f) TERS image of $WS_2$ from overlapping 4-NTP and DMAB. Intensity of 1330 and 1563 $cm^{-1}$ band of 4-NTP is shown in blue and green; and intensity of 1387, 1437, and 1468 $cm^{-1}$ band (azo vibration) of DMAB is shown in red. (g) Corresponding AFM image of $WS_2$. The scanning step size was 10 nm per pixel, spectral acquisition time was 0.5 s.

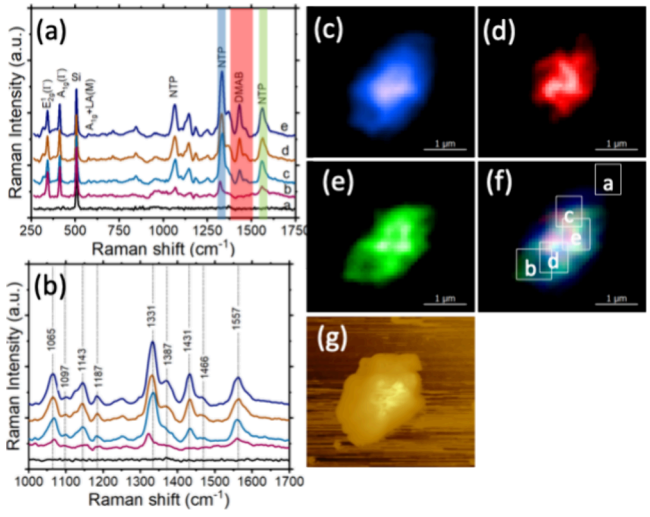


**Figure 3.** (a) Catalytic reactivity of $WS_2$@PdNPs. TER spectra extracted from chemical maps on 4-NTP decorated $WS_2$@PdNPs: (b) showing the presence of 4-NTP and DMAB. (c–f) TERS image of $WS_2$ with (c) and (e) 4-NTP and (d) DMAB. (f) TERS image of $WS_2$ from overlapping 4-NTP and DMAB. Intensity of 1331 and 1557 $cm^{-1}$ band of 4-NTP is shown in blue and green; and intensity of 1387, 1431, and 1466 $cm^{-1}$ band (azo vibration) of DMAB is shown in red. (g) Corresponding AFM image of $WS_2$@PdNPs. The scanning step size was 10 nm per pixel, spectral acquisition time was 0.5 s.

DMAB formation. To verify this hypothesis, we performed nano-infrared analysis of $WS_2$ nanoplates with 4-NTP on their surface. Nano-IR imaging confirmed the presence of DMAB (1435 and 1465 $cm^{-1}$) on the surface of $WS_2$ nanoplates that were never explored by TERS, as shown in Figure S2.

TERS imaging of $WS_2$@PdNPs exposed to 4-NTP revealed a much greater yield of DMAB on their surface compared to $WS_2$, Figure 3. This conclusion could be made by very strong intensities of 1431 and 1466 $cm^{-1}$ that could be assigned to DMAB in TERS spectra acquired from various parts of $WS_2$@PdNPs, Figure 3. Similar to $WS_2$, we found that central parts of $WS_2$@Pd nanoplates exhibited greater intensity of DMAB vibrational bands compared to the edges of $WS_2$@Pd hybrids. These results show that central parts of $WS_2$@Pd have greater photocatalytic reactivity compared to edges of $WS_2$@PdNPs. This observation could be explained by the higher density of PdNPs in the central parts of these nanostructures. Although PdNPs alone could not catalyze the dimerization of 4-NTP into DMAB, the coupling of PdNPs with $WS_2$ yielded a highly efficient catalyst in which PdNPs played a critically important role.

It should be noted that vibrational signatures of DMAB were also evident in the nano-IR spectra acquired from the surface of $WS_2$@PdNPs exposed to 4-NTP, as shown in Figure 4. These results indicate that $WS_2$@PdNPs rather than the metallic scanning probe used in TERS were capable of photo reducing 4-NTP into DMAB. Similar to TERS, nano-IR revealed a much stronger intensity of 1448 $cm^{-1}$ in the nano-IR spectra acquired from $WS_2$@PdNPs to $WS_2$. These results indicate that $WS_2$@PdNPs enabled much greater photo-conversion of 4-NTP into DMAB.

To further investigate photocatalytic reactivity of $WS_2$ and $WS_2$@PdNPs, we quantified the yield of DMAB at different power of $\lambda$ = 633 nm laser light (2.9 $\mu$W-140 $\mu$W), Figure S3 and Figure S4. We determined the number of TERS spectra

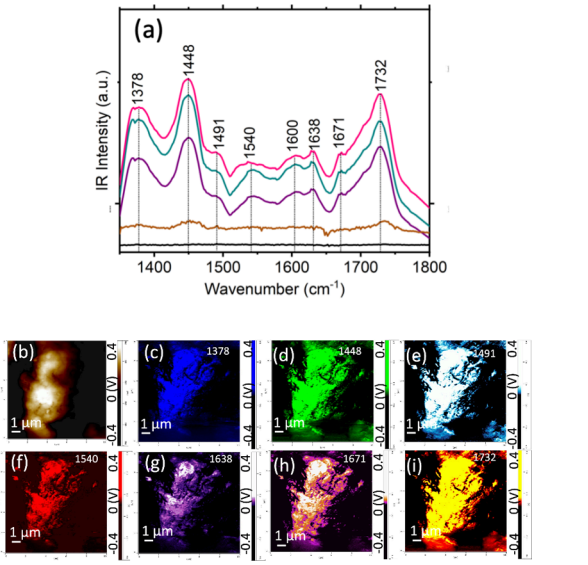


**Figure 4.** AFM-IR spectra acquired from the surface of $WS_2$@PdNPs decorated with 4-NTP (a), AFM image of $WS_2$@PdNPs (b) and chemical images (c-i) of $WS_2$@PdNPs revealing localization of 4-NTP and DMAB.

that exhibit the vibrational signatures of 4-NTP and DMAB under each of these experimental conditions. Our results show that with an increase in the laser power, the yield of DMAB increased with a gradual decrease in the concentration of 4-NTP on the nanoplate surfaces, Figure 5, a-b. It should be noted that a nearly linear relationship between the yield of DMAB and the laser power was observed for the $WS_2$ nanoplates. However, a rapid decline in the concentration of 4-NTP on $WS_2$@PdNPs was observed with an increase in the lase power. We also observed no changes in the concentration of both 4-NTP and DMAB on $WS_2$@Pd above 60 $\mu$W of $\lambda$ =


https://doi.org/10.1021/acs.nanolett.4c03702
Nano Lett. 2024, 24, 13004−13009

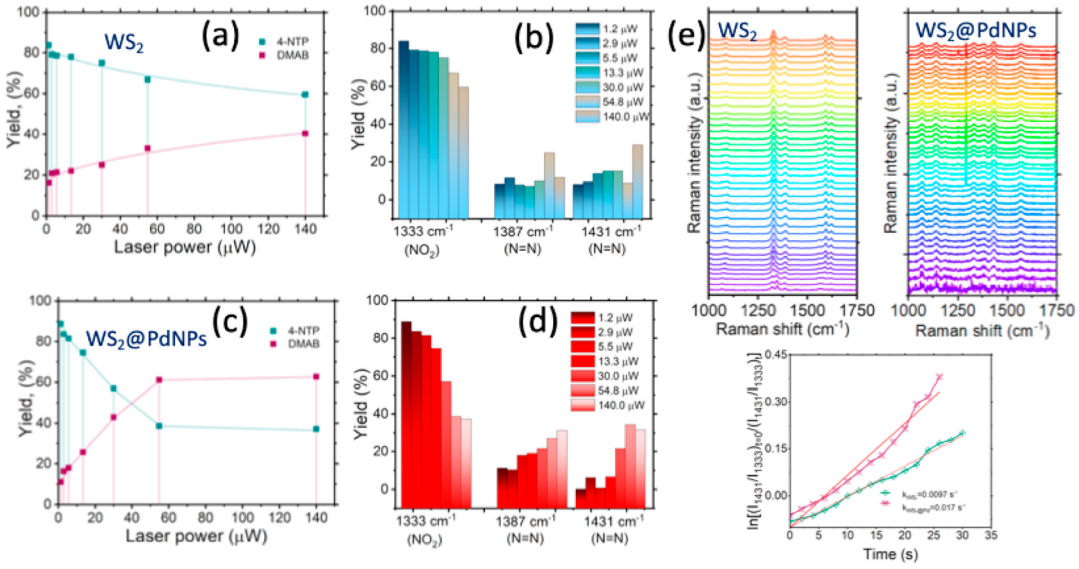


**Figure 5.** Graphs (a and c) and histograms (b and d) of changes in the concentration of 4-NTP and DMAB on the surface of $WS_2$ (a and b) and $WS_2$@Pd (c and d) at different powers of $\lambda$ = 633 nm laser light. (e) Waterfall maps of 4-NTP to DMAB reduction on the surface of $WS_2$ and $WS_2$@Pd nanoplates. Rate constants of 4-NTP to DMAB reduction are based on the intensity ratio of the bands of 1431 $cm^{-1}$ (DMAB) and 1330 $cm^{-1}$ ($NO_2$) in TERS spectra obtained from $WS_2$ and $WS_2$@Pd with 4-NTP on their surfaces. Each trace was fitted with a linear model according to eq 1.

633 nm light. Comparison of the yield of DMAB on $WS_2$@PdNPs and on the $WS_2$ nanoplates indicates that at low laser powers (2.9−20 $\mu$W), comparable yield of DMAB was observed on both nanostructures. However, above 20 $\mu$W, $WS_2$@PdNPs demonstrated far more superior yield od DMAB compared to $WS_2$, Figure 5, c-d.

Finally, we performed kinetic measurements of 4-NTP to DMAB conversion to determine the rate of photocatalytic reactions on $WS_2$ and $WS_2$@PdNPs. For this, we determined a change in intensities of 1431 $cm^{-1}$ (DMAB) vs 1330 $cm^{-1}$ (4-NTP) and plotted a natural logarithm of their ratio at different points, eq 1, Figure 5, e.[35] We found that an increase in the light intensity causes the increase in the reaciton rate of 4-NTP to DMAB conversion on both $WS_2$ and $WS_2$@Pd nanoplates. Our results show that $k_{WS2}$ = 0.0097 $s^{-1}$, whereas $k_{WS2@Pd}$ = 0.017 $s^{-1}$. Thus, although rates of photoconversion of 4-NTP to DMAB were very similar on $WS_2$ nanoplates, $WS_2$@Pd hybrids demonstrated higher rates of photocatalysis compared to unmodified 2D dichalcogenides. This first-order kinetic relationship observed for DMAB formation on $WS_2$ nanoplates and $WS_2$@PdNPs hybrids suggests that the their surfaces could possess both covalently (Au−S) anchored 4-NBT and an excess of unbound 4-NBT.[27] In this case, the rate of the reaction is determined by covalently bound 4-NBT. Thus, the dimerization of 4-NBT is a pseudo first-order reaction. These results also indicate that molecular orientation on the surface of both $WS_2$ and $WS_2$@PdNPs could play an important role in the catalytic reactivity of these nanostructures.

$$\ln\left[\frac{(c_{(4-NBT)})t_0}{(c_{(4-NBT)})t}\right] = \ln\left[\frac{(I_{1431}/I_{1330})t_0}{(I_{1431}/I_{1330})t}\right] = kt \quad (1)$$

where $c(4\text{-NTP})_{t0}$ and $c(4\text{-NTP})_t$ represent the concentration of 4-NTP at different reaction time. $I_{1431}$ and $I_{1330}$ are the intensities of the bands at 1431 $cm^{-1}$(DMAB) and 1330 $cm^{-1}$($NO_2$), respectively. $k$ is the rate constant, and $t$ is the reaction time.

Both the Brus and Jain laboratories demonstrated that illumination of noble metal nanostructures by light results in the appearance of a steady-state charge of their surfaces.[28−31] The charge originates from unequal rates of dissipation of hot electrons and holes from the metal surface. This asymmetry results in an accumulation of hot carriers with lower transfer rates between the nanostructures and the surrounding medium. Using benzonitrile as a molecular reporter, our group quantified the magnitude of the steady-state charge on the surface of mono- and bimetallic nanostructures.[32] Using TERS, we also demonstrated that the magnitude of the charge, and consequently reactivity of these nanostructures, could be altered by the intensity of the laser light.[32] These results are in a good agreement with experimental and theoretical evidence reported by Jain's group according to which a steady-state potential can be viewed as the driving force of chemical reactions.[29−31]

Illumination of 2D dichalcogenides results in the formation of excitons and trions,[33−35] which, in turn can dissipate forming a steady-state charge on the surface of $WS_2$ and $WS_2$@Pd nanoplates. We hypothesize that this steady-state charge, also described as photopotential by the Lagugné-Labarthet group,[19] can drive the dimerization of 4-NTP into DMAB. Our results also suggest that PdNPs confine the charge which results in the superior reactivity of $WS_2$@PdNPs compared to $WS_2$. Alternatively, excitons formed on $WS_2$ and $WS_2$@Pd nanoplates can directly trigger the observed chemical transformation in 4-NTP. Additional studies are required to disentangle these two possible catalytic mechanisms. This work is currently in progress in our group.

## CONCLUSION

Our results indicate that light-induced excitons on $WS_2$ and $WS_2$@PdNPs coupled were capable of reducing 4-NTP into DMAB. We also found that central parts of both $WS_2$ and $WS_2$@Pd nanoplates exhibit much stronger photocatalytic properties compared to their edges. Using TERS, we were able


https://doi.org/10.1021/acs.nanolett.4c03702
Nano Lett. 2024, 24, 13004−13009

to determine the relationship between light power, rate, and yields of photocatalytic reactions on the surface of $WS_2$ and $WS_2$@PdNPs. Our results indicate that $WS_2$@PdNPs demonstrate a very similar yield of DMAB at low laser powers (2.9–20 $\mu$M). However, a superior yield of DMAB was observed on $WS_2$@Pd compared to $WS_2$ nanoplates at the laser powers above 20 $\mu$M. Thus, our results indicate that catalytic performance of $WS_2$ nanoplates could be enhanced by Pd nanoparticles.

## ■ ASSOCIATED CONTENT

### Supporting Information

The Supporting Information is available free of charge at https://pubs.acs.org/doi/10.1021/acs.nanolett.4c03702.

Additional experimental details, materials, and methods are summarized in Supporting Information. Figure S1 shows TER spectra of $WS_2$@PdNPs; Figure S2 summarizes results of AFM-IR imaging of the surface of $WS_2$nanoplates coated by 4-NTP. Figure S3 and S4 show TERS spectra acquired from WS2 and WS2@PdNPs modified by 4-NTP at different laser light intensities (PDF)

## ■ AUTHOR INFORMATION


### Corresponding Author

**Dmitry Kurouski** − *Department of Biochemistry and Biophysics, Texas A&M University, College Station, Texas 77843, United States; Department of Biomedical Engineering, Texas A&M University, College Station, Texas 77843, United States;* orcid.org/0000-0002-6040-4213; Phone: 979-458-3778; Email: dkurouski@tamu.edu

### Author

**Swati J. Patil** − *Department of Biochemistry and Biophysics, Texas A&M University, College Station, Texas 77843, United States;* orcid.org/0000-0002-3619-2783

Complete contact information is available at: https://pubs.acs.org/10.1021/acs.nanolett.4c03702


### Author Contributions

The manuscript was written through contributions of all authors. All authors have given approval to the final version of the manuscript.

### Notes

The authors declare no competing financial interest.

## ■ ACKNOWLEDGMENTS

We are grateful to AgriLife Research of Texas A&M for financial support. We also acknowledge the Governor's University Research Initiative (GURI) grant program of Texas A&M University, GURI Grant Agreement No. 12-2016, M1700437.

## ■ REFERENCES


(1) Sharma, B.; Frontiera, R. R.; Henry, A. I.; Ringe, E.; Van Duyne, R. P. SERS: Materials, applications, and the future. *Mater. Today* **2012**, *15* (1–2), 16–25.

(2) Xiao, L.; Schultz, Z. D. Spectroscopic Imaging at the Nanoscale: Technologies and Recent Applications. *Anal. Chem.* **2018**, *90* (1), 440–458.

(3) Xie, W.; Schlucker, S. Surface-enhanced Raman spectroscopic detection of molecular chemo- and plasmo-catalysis on noble metal nanoparticles. *Chem. Commun.* **2018**, *54*, 2326–2336.

(4) Moskovits, M. Surface roughness and the enhanced intensity of Raman scattering by molecules adsorbed on metals. *J. Chem. Phys.* **1978**, *69* (9), 4159–4161.

(5) King, F. W.; Van Duyne, R. P.; Schatz, G. C. Theory of Raman scattering by molecules adsorbed on electrode surfaces. *J. Chem. Phys.* **1978**, *69* (10), 4472–4481.

(6) Wustholz, K. L.; Henry, A.-I.; McMahon, J. M.; Freeman, R. G.; Valley, N.; Piotti, M. E.; Natan, M. J.; Schatz, G. C.; Van Duyne, R. P. Structure- activity relationships in gold nanoparticle dimers and trimers for surface-enhanced Raman spectroscopy. *J. Am. Chem. Soc.* **2010**, *132* (31), 10903–10910.

(7) Jeanmaire, D. L.; Van Duyne, R. P. Surface raman spectroelectrochemistry: Part I. Heterocyclic, aromatic, and aliphatic amines adsorbed on the anodized silver electrode. *J. Electroanal. Chem.* **1977**, *84* (1), 1–20.

(8) Brongersma, M. L.; Halas, N. J.; Nordlander, P. Plasmon-induced hot carrier science and technology. *Nat. Nanotechnol.* **2015**, *10* (1), 25–34.

(9) Brown, A. M.; Sundararaman, R.; Narang, P.; Goddard, W. A., III; Atwater, H. A. Nonradiative plasmon decay and hot carrier dynamics: effects of phonons, surfaces, and geometry. *ACS Nano* **2016**, *10* (1), 957–966.

(10) Cortés, E.; Xie, W.; Cambiasso, J.; Jermyn, A. S.; Sundararaman, R.; Narang, P.; Schlücker, S.; Maier, S. A. Plasmonic hot electron transport drives nano-localized chemistry. *Nat. Commun.* **2017**, *8*, 14880.

(11) Huh, H.; Trinh, H. D.; Lee, D.; Yoon, S. How Does a Plasmon-Induced Hot Charge Carrier Break a C-C Bond? *ACS Appl. Mater. Interfaces* **2019**, *11* (27), 24715–24724.

(12) Wang, F.; Li, C.; Chen, H.; Jiang, R.; Sun, L. D.; Li, Q.; Wang, J.; Yu, J. C.; Yan, C. H. Plasmonic harvesting of light energy for Suzuki coupling reactions. *J. Am. Chem. Soc.* **2013**, *135* (15), 5588–5601.

(13) Zhou, L.; Martirez, J. M. P.; Finzel, J.; Zhang, C.; Swearer, D. F.; Tian, S.; Robatjazi, H.; Lou, M.; Dong, L.; Henderson, L.; et al. Light-driven methane dry reforming with single atomic site antenna-reactor plasmonic photocatalysts. *Nature Energy* **2020**, *5*, 61–70.

(14) Sytwu, K.; Vadai, M.; Dionne, J. A. Bimetallic nanostructures: combining plasmonic and catalytic metals for photocatalysis. *Adv. Phys.* **2019**, *4* (1), 1619480.

(15) Li, Z.; Kurouski, D. Probing the Redox Selectivity on Au@Pd and Au@Pt Bimetallic Nanoplates by Tip-Enhanced Raman Spectroscopy. *Acs Photonics* **2021**, *8* (7), 2112–2119.

(16) Li, Z.; Kurouski, D. Probing the plasmon-driven Suzuki-Miyaura coupling reactions with cargo-TERS towards tailored catalysis. *Nanoscale* **2021**, *13* (27), 11793–11799.

(17) Li, Z.; Kurouski, D. Tip-Enhanced Raman Analysis of Plasmonic and Photocatalytic Properties of Copper Nanomaterials. *J. Phys. Chem. Lett.* **2021**, *12* (34), 8335–8340.

(18) Patil, S. J.; Kurouski, D. Tip-enhanced Raman imaging of plasmon-driven dimerization of 4-bromothiophenol on nickel-decorated gold nanoplate bimetallic nanostructures. *Chem. Commun. (Camb)* **2023**, *59* (73), 10976–10979.

(19) Lambin, C.; Avilés, M. O.; Jelken, J.; Lagugné-Labarthet, F. Molybdenum Disulfide Flakes as Platforms for the Photoconversion of 4-Nitrothiophenol. *J. Phys. Chem. C* **2023**, *127* (50), 24281–24290.

(20) Rizevsky, S.; Kurouski, D. Tip-Enhanced Raman Imaging of Photocatalytic Processes at the Nanoscale. *J. Phys. Chem. C* **2022**, *126* (35), 14781–14790.

(21) Zhang, R.; Zhang, Y.; Dong, Z. C.; Jiang, S.; Zhang, C.; Chen, L. G.; Zhang, L.; Liao, Y.; Aizpurua, J.; Luo, Y.; et al. Chemical mapping of a single molecule by plasmon-enhanced Raman scattering. *Nature* **2013**, *498* (7452), 82–86.

(22) Lee, J.; Crampton, K. T.; Tallarida, N.; Apkarian, V. A. Visualizing vibrational normal modes of a single molecule with atomically confined light. *Nature* **2019**, *568* (7750), 78–82.

(23) Tallarida, N.; Lee, J.; Apkarian, V. A. Tip-Enhanced Raman Spectromicroscopy on the Angstrom Scale: Bare and CO-Terminated Ag Tips. *ACS Nano* **2017**, *11* (11), 11393−11401.
(24) Li, Z.; Wang, R.; Kurouski, D. Nanoscale Photocatalytic Activity of Gold and Gold-Palladium Nanostructures Revealed by Tip-Enhanced Raman Spectroscopy. *J. Phys. Chem. Lett.* **2020**, *11*, 5531−5537.
(25) Li, Z.; Kurouski, D. Plasmon-Driven Chemistry on Mono- and Bimetallic Nanostructures. *Acc. Chem. Res.* **2021**, *54* (10), 2477−2487.
(26) Li, Z.; Ehtesabi, S.; Gojare, S.; Richter, M.; Kupfer, S.; Grafe, S.; Kurouski, D. Plasmon-Determined Selectivity in Photocatalytic Transformations on Gold and Gold-Palladium Nanostructures. *ACS Photonics* **2023**, *10* (9), 3390−3400.
(27) Cai, Z. F.; Merino, J. P.; Fang, W.; Kumar, N.; Richardson, J. O.; De Feyter, S.; Zenobi, R. Molecular-Level Insights on Reactive Arrangement in On-Surface Photocatalytic Coupling Reactions Using Tip-Enhanced Raman Spectroscopy. *J. Am. Chem. Soc.* **2022**, *144* (1), 538−546.
(28) Redmond, P. L.; Brus, L. E. "Hot Electron" Photo-Charging and Electrochemical Discharge Kinetics of Silver Nanocrystals. *J. Phys. Chem. C* **2007**, *111*, 14849−11485.
(29) Wilson, A. J.; Jain, P. K. Light-Induced Voltages in Catalysis by Plasmonic Nanostructures. *Acc. Chem. Res.* **2020**, *53*, 1773−1781.
(30) Yu, S.; Jain, P. K. The Chemical Potential of Plasmonic Excitations. *Angew. Chem., Int. Ed.* **2020**, *59*, 2085−2088.
(31) Yu, S.; Wilson, A. J.; Heo, J.; Jain, P. K. Plasmonic Control of Multi-Electron Transfer and C-C Coupling in Visible-Light-Driven CO2 Reduction on Au Nanoparticles. *Nano Lett.* **2018**, *18*, 2189−2194.
(32) Li, Z.; Rigor, J.; Large, N.; El-Khoury, P.; Kurouski, D. Underlying Mechanisms of Hot Carrier-Driven Reactivity on Bimetallic Nanostructures. *J. Phys. Chem. C* **2021**, *125*, 2492−2501.
(33) Park, K. D.; Jiang, T.; Clark, G.; Xu, X.; Raschke, M. B. Radiative control of dark excitons at room temperature by nano-optical antenna-tip Purcell effect. *Nat. Nanotechnol* **2018**, *13* (1), 59−64.
(34) Park, K. D.; Khatib, O.; Kravtsov, V.; Clark, G.; Xu, X.; Raschke, M. B. Hybrid Tip-Enhanced Nanospectroscopy and Nanoimaging of Monolayer WSe2 with Local Strain Control. *Nano Lett.* **2016**, *16* (4), 2621−2627.
(35) Park, K. D.; Muller, E. A.; Kravtsov, V.; Sass, P. M.; Dreyer, J.; Atkin, J. M.; Raschke, M. B. Variable-Temperature Tip-Enhanced Raman Spectroscopy of Single-Molecule Fluctuations and Dynamics. *Nano Lett.* **2016**, *16* (1), 479−487.


https://doi.org/10.1021/acs.nanolett.4c03702
*Nano Lett.* 2024, 24, 13004−13009